

OPEN ACCESS

## Breakdown up to 13.5 kV in NiO/ $\beta$ -Ga<sub>2</sub>O<sub>3</sub> Vertical Heterojunction Rectifiers

To cite this article: Jian-Sian Li *et al* 2024 *ECS J. Solid State Sci. Technol.* **13** 035003

View the [article online](#) for updates and enhancements.

### You may also like

- [A landscape of  \$\beta\$ -Ga<sub>2</sub>O<sub>3</sub> Schottky power diodes](#)  
Man Hoi Wong
- [Low on-resistance 1.2 kV 4H-SiC power MOSFET with  \$R\_{DS\(on\)}\$  of 3.4 m \$\cdot\$ cm<sup>2</sup>](#)  
Qiang Liu, Qian Wang, Hao Liu et al.
- [Dependence of reverse leakage on the edge termination process in vertical GaN power device](#)  
Tailang Xie, Cláudia da Silva, Nadine Szabó et al.



### Your Lab in a Box!

The PAT-Tester-i-16: All you need for Battery Material Testing.

- ✓ All-in-One Solution with integrated Temperature Chamber!
- ✓ Cableless Connection for Battery Test Cells!
- ✓ Fully featured Multichannel Potentiostat / Galvanostat / EIS!

[www.el-cell.com](http://www.el-cell.com) +49 40 79012-734 [sales@el-cell.com](mailto:sales@el-cell.com)

**EL-CELL**<sup>®</sup>  
electrochemical test equipment





# Breakdown up to 13.5 kV in NiO/ $\beta$ -Ga<sub>2</sub>O<sub>3</sub> Vertical Heterojunction Rectifiers

Jian-Sian Li,<sup>1,\*</sup> Hsiao-Hsuan Wan,<sup>1,\*</sup> Chao-Ching Chiang,<sup>1,\*</sup> Timothy Jinsoo Yoo,<sup>2</sup> Meng-Hsun Yu,<sup>3</sup> Fan Ren,<sup>1,\*\*</sup> Honggyu Kim,<sup>2</sup> Yu-Te Liao,<sup>3</sup> and Stephen J. Pearton<sup>2,\*,z</sup>

<sup>1</sup>Department of Chemical Engineering, University of Florida, Gainesville, Florida 32606 United States of America

<sup>2</sup>Department of Materials Science and Engineering, University of Florida, Gainesville, Florida 32606 United States of America

<sup>3</sup>Department of Electronics and Electrical Engineering, National Yang Ming Chiao Tung University, Hsinchu 30010, Taiwan

Vertical heterojunction NiO/ $\beta$ -Ga<sub>2</sub>O<sub>3</sub>/n<sup>+</sup>-Ga<sub>2</sub>O<sub>3</sub> rectifiers with 100  $\mu$ m diameter fabricated on  $\sim$ 17–18  $\mu$ m thick drift layers with carrier concentration  $8.8 \times 10^{15} \text{ cm}^{-3}$  and employing simple dual-layer PECVD SiNx/SiO<sub>2</sub> edge termination demonstrate breakdown voltages ( $V_B$ ) up to 13.5 kV, on-voltage ( $V_{ON}$ ) of  $\sim$ 2.2 V and on-state resistance  $R_{ON}$  of 11.1–12 m $\Omega \cdot \text{cm}^2$ . Without edge termination, the maximum  $V_B$  was 7.9 kV. The average critical breakdown field in heterojunctions was  $\sim$ 7.4–9.4 MV  $\cdot \text{cm}^{-1}$ , within the reported theoretical value range from 8–15 MV  $\cdot \text{cm}^{-1}$  for  $\beta$ -Ga<sub>2</sub>O<sub>3</sub>. For large area (1 mm diameter) heterojunction devices, the maximum  $V_B$  was 7.2 kV with optimized edge termination and 3.9 kV without edge termination. The associated maximum power figure-of-merit,  $V_B^2/R_{ON}$  is 15.2 GW  $\cdot \text{cm}^{-2}$  for small area devices and 0.65 GW  $\cdot \text{cm}^{-2}$  for large area devices. By sharp contrast, small area Schottky rectifiers concurrently fabricated on the same drift layers had maximum  $V_B$  of 3.6 kV with edge termination and 2.7 kV without edge termination, but lower  $V_{ON}$  of 0.71–0.75 V. The average critical breakdown field in these devices was in the range 1.9–2.7 MV  $\cdot \text{cm}^{-1}$ , showing the importance of both the heterojunction and edge termination. Transmission electron microscopy showed an absence of lattice damage between the PECVD and sputtered films within the device and the underlying epitaxial Ga<sub>2</sub>O<sub>3</sub>. The key advances are thicker, lower doped drift layers and optimization of edge termination design and deposition processes.

© 2024 The Author(s). Published on behalf of The Electrochemical Society by IOP Publishing Limited. This is an open access article distributed under the terms of the Creative Commons Attribution 4.0 License (CC BY, <http://creativecommons.org/licenses/by/4.0/>), which permits unrestricted reuse of the work in any medium, provided the original work is properly cited. [DOI: 10.1149/2162-8777/ad3457]



Manuscript submitted February 14, 2024; revised manuscript received March 1, 2024. Published March 27, 2024.

There has been rapid progress in Ga<sub>2</sub>O<sub>3</sub> power rectifiers since the initial demonstration of a 1 kV device in 2017.<sup>1</sup> This has included improved edge termination methods and the use of NiO as a p-type layer to realize heterojunctions with much higher breakdown voltages than conventional Schottky rectifiers.<sup>2–15</sup> For most power switching applications, vertical devices are preferred. In contrast to lateral geometries,<sup>16–18</sup> the breakdown voltage ( $V_B$ ) of vertical Schottky Barrier Diodes (SBDs) exhibits a proportional relationship with the thickness of the drift layer, as opposed to the lateral separation between the anode and cathode.<sup>19–23</sup> This relationship results in an augmented power density or an increased blocking voltage while minimizing the chip's spatial footprint. Furthermore, vertical devices demonstrate a more uniform heat distribution due to enhanced current spreading characteristics. To fully harness the potential of these devices, it is imperative to develop appropriate edge termination designs suitable for integration into NiO/ $\beta$ -Ga<sub>2</sub>O<sub>3</sub> devices.<sup>24–39</sup> Such designs aim to restrict the maximum electric field magnitude surrounding the periphery of the rectifying contact. Potential applications for these power devices include EV charging systems, motor control and grid-scale power switching because of the excellent dc power, switching and high temperature performance.<sup>40–51</sup> Ga<sub>2</sub>O<sub>3</sub> may also be a potential candidate for high power density switched mode RF amplifiers.

There have been numerous studies to identify the crystal defects that contribute to reverse leakage current in Ga<sub>2</sub>O<sub>3</sub> rectifiers.<sup>52–65</sup> The emergence of leakage current can be ascribed to the existence of many types of such crystal defects in HVPE layers.<sup>53–57</sup> These include polycrystalline anomalies,<sup>55</sup> stacking faults and probe-induced surface defects,<sup>65</sup> line-shaped imperfections,<sup>52</sup> and various types of dislocations and other oriented crystal anomalies,<sup>63</sup> all of which function as conduits for reverse leakage currents in the thick drift regions grown by halide vapor phase epitaxy on (001)  $\beta$ -Ga<sub>2</sub>O<sub>3</sub> substrates for Schottky barrier diodes (SBDs).<sup>66</sup>

While there have been many studies of the current transport mechanisms, selection of different materials in the field plates and the effect of field mitigation methods such as beveling, guard rings or charge compensation on the field distribution, there are still some obvious issues from the literature that, if optimized, would produce higher breakdown voltages. The first is that the Ga<sub>2</sub>O<sub>3</sub> surface is sensitive to ion-induced damage.<sup>67</sup> This is exploited to lower the Ohmic contact resistance,<sup>2–4</sup> but clearly, is detrimental to rectifying contacts. Thus, ion-induced damage must be minimized during deposition of the NiO p-layer in the heterojunction and similarly with field plate structures, commonly deposited by plasma-enhanced chemical vapor deposition. The second area of focus is realization of thicker, lower-doped drift regions. Since recent results have shown average electric fields near the theoretical maximum in Ga<sub>2</sub>O<sub>3</sub>,<sup>13,32,48,51</sup> then achievement of thicker layers while maintaining low background carrier concentration is key.

In this paper, we show that the use of lightly doped 17–18  $\mu$ m drift layers, combined with low damage deposition of NiO and optimized design and deposition of dual layer field plates can produce breakdown voltages up to 13.5 kV in NiO/Ga<sub>2</sub>O<sub>3</sub> heterojunction rectifiers of diameter 100  $\mu$ m and 7.2 kV in 1 mm diameter devices. This is in excess of the 1D breakdown limit of both SiC and GaN of similar drift layer thickness and the simple device structure does not need mesa etching or implantation steps.

## Experimental

The starting structures were in the range 17.7–18.2  $\mu$ m thick, lightly doped ( $8.8 \times 10^{15} \text{ cm}^{-3}$ ) drift layers grown by Halide Vapor Phase Epitaxy (HVPE) on heavily doped n-type substrates (Sn-doped, (001),  $10^{19} \text{ cm}^{-3}$ ) grown by Edge-Defined Film-Fed Growth. Mapping of the epi thickness showed a variation from a minimum of 17.7 to a maximum of 18.2  $\mu$ m, with an average of 16.1  $\mu$ m. The doping was uniform across the whole wafer diameter. Full-area backside Ohmic contacts were deposited by e-beam evaporation of Ti/Au subsequently annealed at 550 °C for 3 min. Both Schottky barrier diodes (SBD) and heterojunction diodes (HJD) were fabricated on the same wafer, with the schematic structures shown in

\*Electrochemical Society Student Member.

\*\*Electrochemical Society Fellow.

<sup>z</sup>E-mail: [spear@mse.ufl.edu](mailto:spear@mse.ufl.edu)

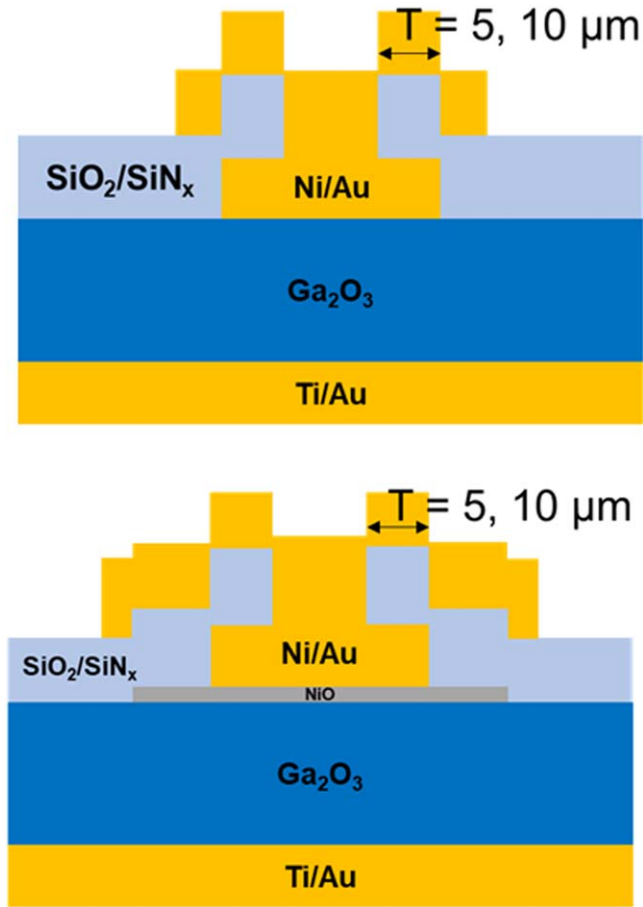


**Figure 1.** Schematic of (top) SBD and (bottom) HJD device structures with edge termination.

Fig. 1. Ni/Au deposited by e-beam evaporation was used as the metal stack in both cases, with the HJD also including a bilayer of NiO deposited by low power sputtering. The respective doping concentrations were  $2.6 \times 10^{18} \text{ cm}^{-3}$  for the top 10 nm thick layer and  $10^{18} \text{ cm}^{-3}$  for the 10 nm bottom layer. Field plates consisting of bilayer  $\text{SiN}_x/\text{SiO}_2$  dielectric that extended  $28 \mu\text{m}$  beyond the Ni/Au were deposited by plasma enhanced chemical vapor deposition. In Fig. 1, T5 and T10 are the distances in  $\mu\text{m}$  from the edge of the dielectric layer and the contact metal. In the HJD, the extension of the NiO beyond the metal contact provides a guard ring for additional edge termination. Details of the design and performance of such bilayer structures were given previously.<sup>68</sup> We have also published a detailed study using TCAD of the electric field distribution for different NiO parameters, including the doping, thickness and extension beyond the anode.<sup>69</sup> These parameters determine where spatially the breakdown can occur, i.e. from the edge of the bilayer NiO extension to directly at the periphery of the top contact, consistent with experimental results.

To quantify the effect of edge termination, we also fabricated SBDs and HJDs without any edge termination, on the same wafer. These are shown in the schematics in Fig. 2. Typically, the breakdown voltages of these devices were approximately half of the values in the edge terminated structures.

Cross-sectional lamella for scanning transmission electron microscopy (STEM) were fabricated using a Ga ion-based FEI Helios Nanolab 600I Dual Beam focused ion beam (FIB)/scanning electron microscopy (SEM) system. The subsequent STEM imaging was performed using an aberration-corrected Themis Z STEM. A high-angle annular dark-field (HAADF) detector was used to obtain Z-contrast, atomic resolution image where heavier elements appear brighter. Energy Dispersive Spectrometry (EDS) analysis in the

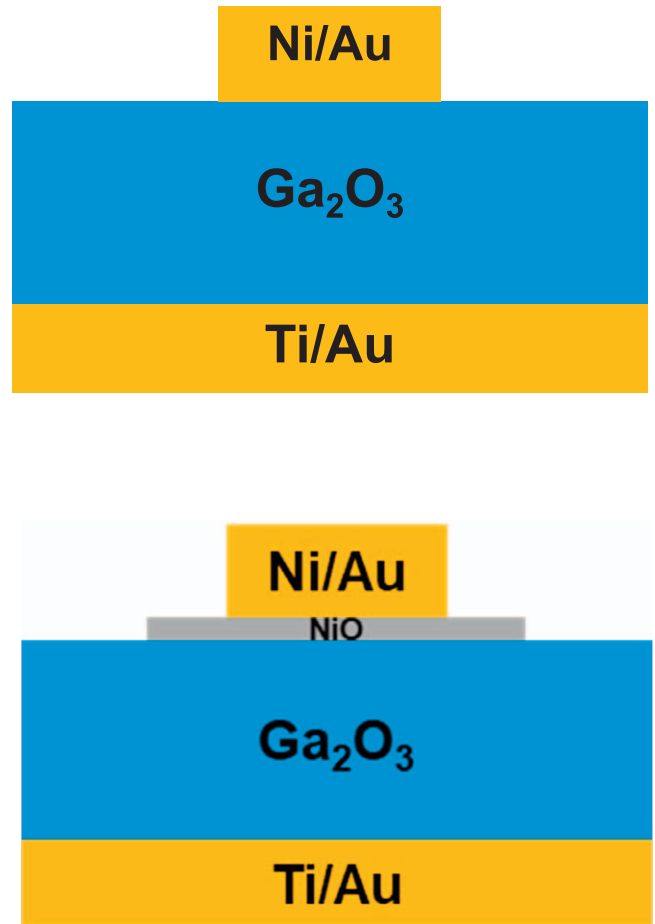


**Figure 2.** Schematic of (top) SBD and (bottom) HJD device structures without the edge termination structures.

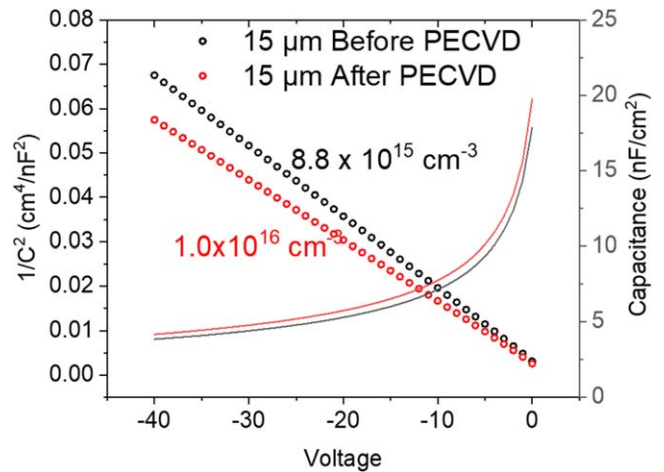


**Figure 3.**  $1/C^2$  -V plots for  $\sim 16 \mu\text{m}$  thick drift layers before and after the PECVD steps to deposit the edge termination layers.

STEM allowed for elemental mapping of the individual layers around the contact stack.

The carrier concentrations in the drift regions of the devices were measured by 1 MHz capacitance-voltage (C-V) measurements and plotting  $1/C^2$ -V plots. The current-voltage (I-V) characteristics were measured under Fluorinert atmospheres at  $25^\circ\text{C}$  using a Tektronix 371-B curve tracer in conjunction with a Glassman high voltage power supply. An Agilent 4156 C parameter analyzer was utilized

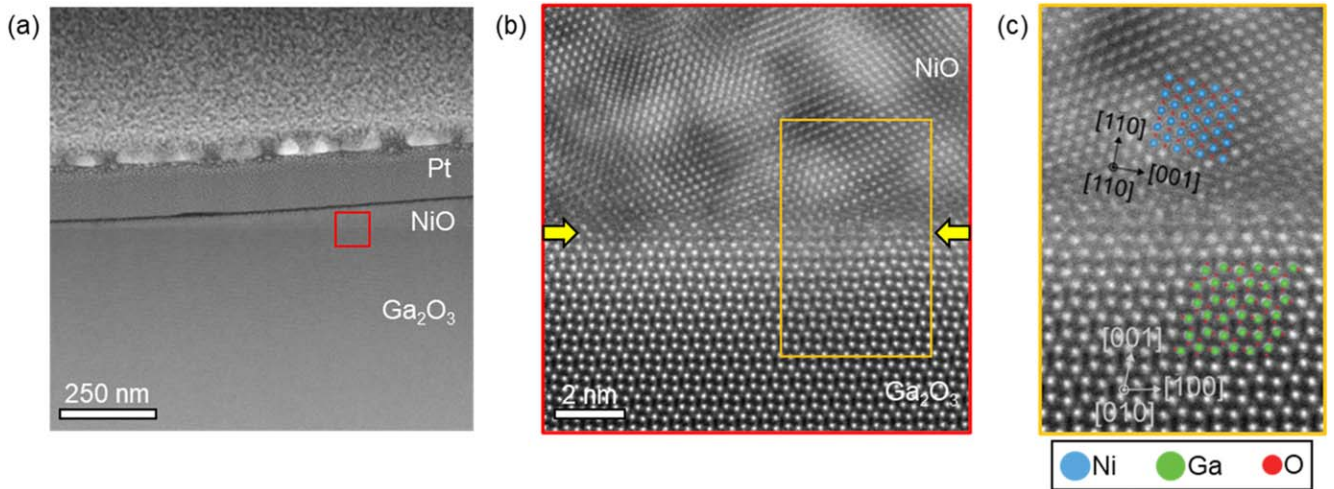


**Figure 4.** (a) Low-magnification HAADF-STEM image of the NiO film bevel edge. The  $\text{Ga}_2\text{O}_3$  substrate, NiO film, and protective Pt straps deposited in the FIB are all visible in this field-of-view. A pristine interface between the NiO and the  $\text{Ga}_2\text{O}_3$  substrate with no visible roughness is observed along the entire edge. (b) High-magnification HAADF-STEM image from the red box in (a) showcasing the atomically abrupt interface marked by yellow arrows. (c) Magnified view of the HAADF-STEM image in (b) from the orange box with corresponding atomic models of the atomic structures of [110] cubic NiO and [010] monoclinic  $\text{Ga}_2\text{O}_3$ .

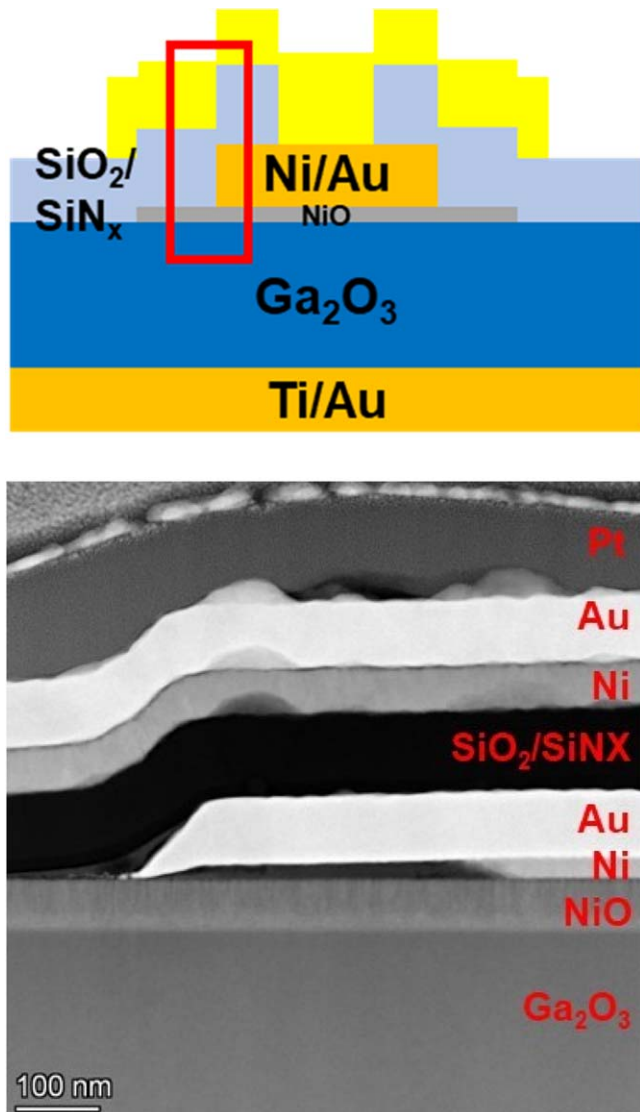


**Figure 5.** Cross-section image of the individual layers around the contact edge.

**Table I. Summary of carrier concentrations and built-in potentials obtained from C-V measurements.**

	Before PECVD	After PECVD
Carrier conc.( $\text{cm}^{-3}$ )	$8.8 \times 10^{15}$	$1.0 \times 10^{16}$
Built-in Potential	2.1	2.4

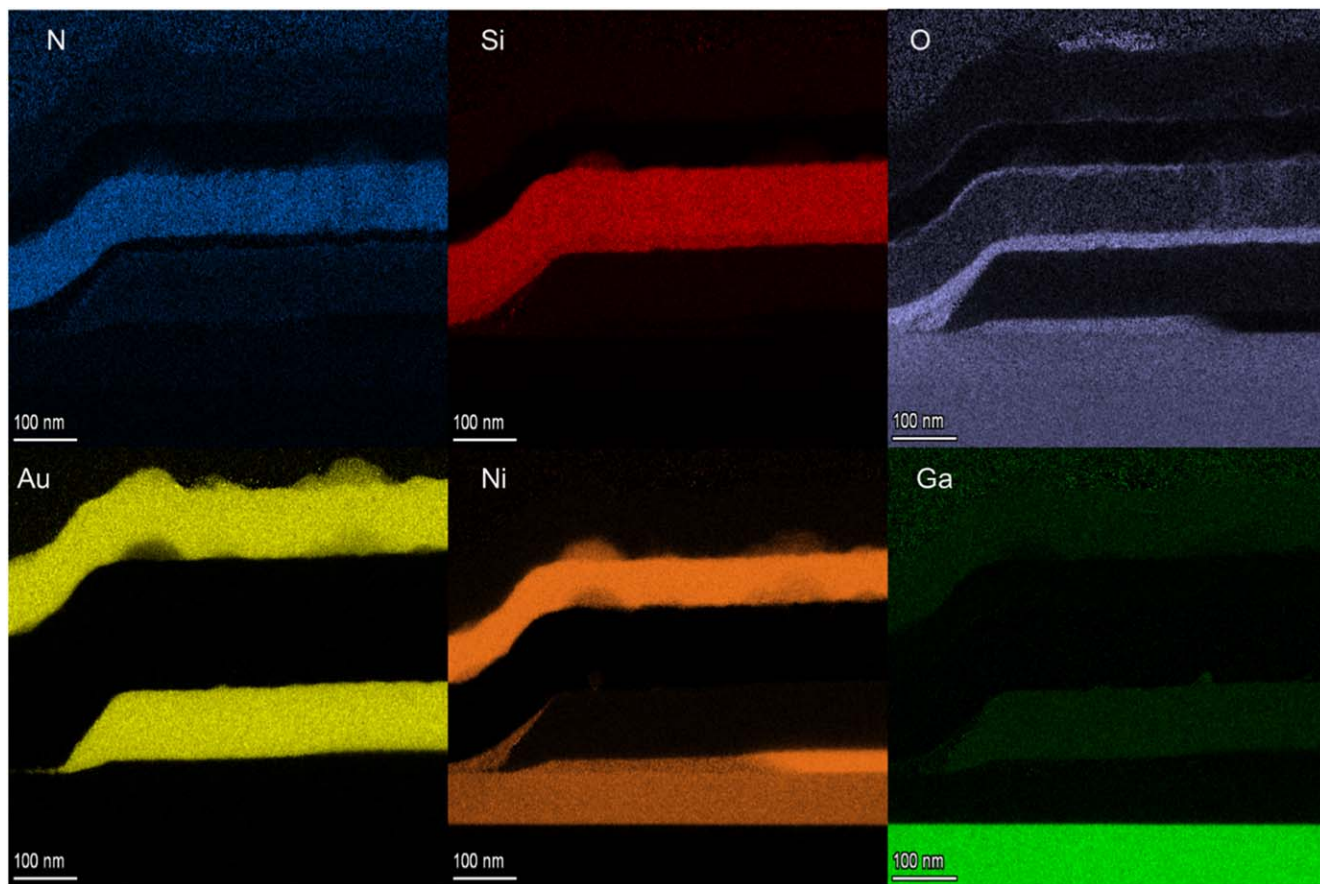
for low voltage forward and reverse current characteristics. The establishment of the reverse breakdown voltage followed the conventional definition, i.e. reverse current reaching  $0.1 \text{ A cm}^{-2}$ . A mega-Ohm resistor was utilized, and the voltage drop across the resistor was subtracted. In addition, the contact was checked every time before the breakdown test by having a forward sweep up to 5 V, the reverse sweep up to  $-100 \text{ V}$  and confirming the I-V. The on-resistance was obtained from the derivative of voltage with respect to current ( $dV/dI$ ) from the I-V characteristics. Corrections were applied to account for the resistance contributed by external circuit components, including cables, chuck, and probe, which collectively amounted to  $10 \Omega$ , which was obtained by measuring the I-V while the cables, chuck and probe were connected together. The typical diode resistances are  $\sim 100 \text{ Ohm}$  at 5 V, which is 10 times the external resistance. The calculated on-resistance values assumed a current spreading length is  $10 \mu\text{m}$ , with a spreading angle of  $45^\circ$ .<sup>32,51</sup> The on-resistance ( $R_{\text{ON}}$ ) typically corresponds to the unipolar drift resistance, which is generally smaller than the diffusion resistance. The I-V characteristics exhibited a high degree of reproducibility over areas measuring  $1 \text{ cm}^2$  on the wafer, with absolute currents having variations of  $<20\%$  at a given voltage.

## Results and Discussion

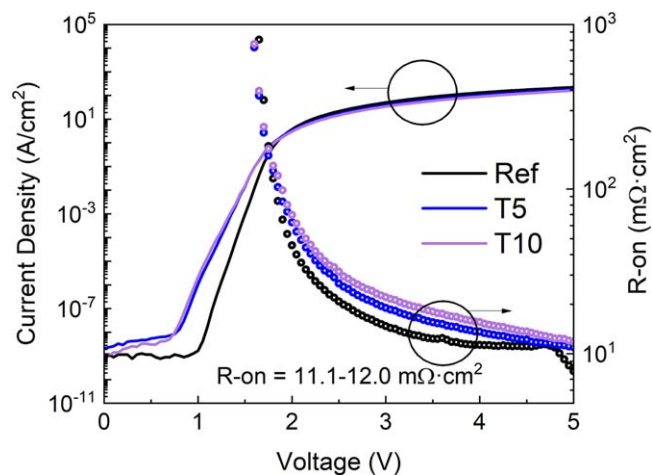
Figure 3 shows the  $1/C^2$  -V plots for  $15 \mu\text{m}$  thick drift layers before and after the PECVD steps to deposit the edge termination layers. The carrier concentrations increase slightly from  $8.8 \times 10^{15} \text{ cm}^{-3}$  prior to the PECVD steps to deposit the dielectric bilayer edge termination. These and the built-in potentials derived from the forward I-V characteristics are summarized in Table I. The increase in carrier density may be a result of incorporation of hydrogen donors during the deposition step. H impurities are easily introduced and have a strong impact on conductivity.<sup>70,71</sup>

Figure 4a shows a low-magnification HAADF-STEM image of the protective Pt/NiO/ $\text{Ga}_2\text{O}_3$  stack before Ni/Au and  $\text{SiO}_2/\text{SiNx}$





**Figure 6.** EDS elemental analysis of layers at the edge of the contact stack.



**Figure 7.** Forward I-V characteristics from HJDs fabricated on  $\sim 16$   $\mu\text{m}$  drift layers. The devices designated Ref do not have edge termination, while the T values are the widths of the edge termination beside the rectifying contact.

layers are deposited. The entire NiO bevel edge maintains a uniform interface with the  $\text{Ga}_2\text{O}_3$  substrate. Figure 4b displays a high-magnification HAADF-STEM image of the red box region in Fig. 4a showing the atomically abrupt interface between the NiO film and the  $\beta\text{-Ga}_2\text{O}_3$  substrate. The [110] orientation of the cubic NiO film is preferentially aligned with the [010] orientation of monoclinic  $\beta\text{-Ga}_2\text{O}_3$  structure. Figure 4c is a further magnified view of the region in the orange box in Fig. 3b with the corresponding atomic models overlayed onto their respective atomic structures. We have previously established the ion energy dependence of dry etch

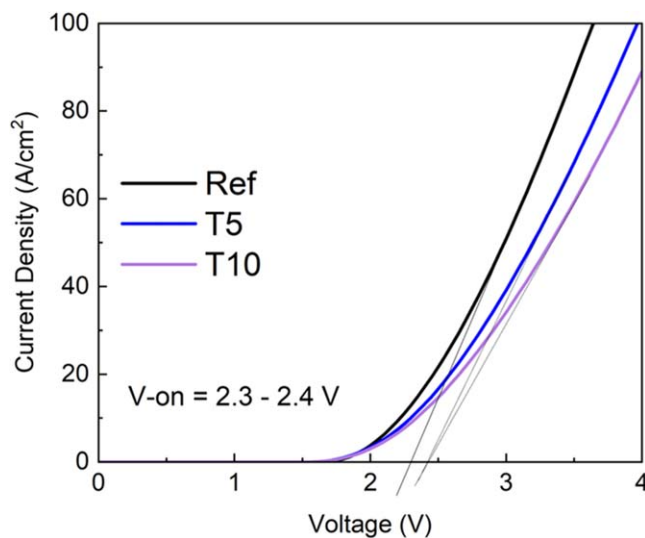


**Figure 8.** Hetero Junction Diode forward I-V characteristic from  $\sim 16$   $\mu\text{m}$  drift layer device on linear scale. Ref is without edge termination but after dielectric layer deposition.

damage depth in  $\text{Ga}_2\text{O}_3$  Schottky rectifiers, in which it is postulated that Ga vacancies created by ion damage compensate the n-type doping in the drift regions and lead to generation-recombination current. Similar comments apply to the PECVD conditions for deposition of the dielectric field plates. We chose low power conditions that had minimal effect on the carrier density in the drift regions, as determined by separate C-V measurements on test structures. There was a slight increase in carrier density after the

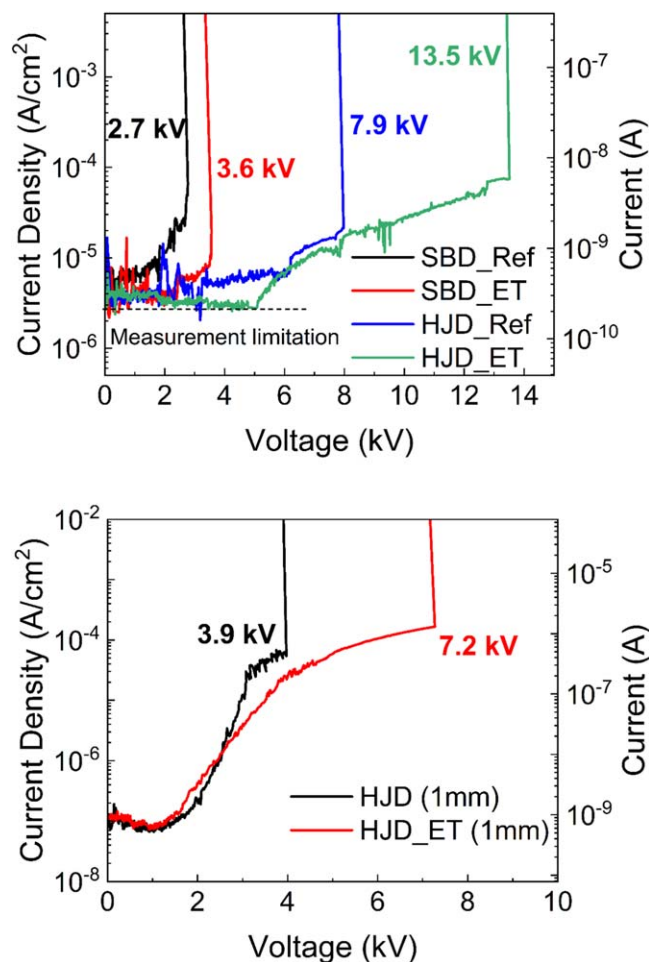


**Figure 9.** (top) Reverse I-V characteristics from 100  $\mu\text{m}$  diameter HJDs and SBDs fabricated on  $\sim 16 \mu\text{m}$  drift layers. This shows the highest  $V_B$  recorded, both with and without edge termination. (bottom) Reverse I-V characteristics from large diameter (1 mm) HJDs with and without edge termination.

PECVD steps for the dielectrics. As mentioned previously, both theory of isolated H properties, as well as experimental evidence show that interstitial hydrogen,  $\text{H}_i$ , is expected to be a shallow donor,  $\text{H}_i^+$ .<sup>70,71</sup>

Figure 5 shows a cross-section image of the area around the contact edge. Note that the first thinner Ni layer on top of NiO film is darker in contrast compared to the upper Ni metal layer. We see from EDS that this region of Ni is oxidized during the processing sequence. For the Ni/Au and  $\text{SiO}_2/\text{SiN}_x$  layers are each  $\sim 100 \text{ nm}$  in height. The quality of films outside of the bevel edge is very good. Figure 6 shows the EDS elemental analysis of the layers at the edge of the contact region. The uppermost Au and Ni layers have some oxidation, and the morphology of those surfaces is rougher than the films closest to the device interface.

Figure 7 shows the forward current density-voltage characteristics from the HJD devices with different spacings. The reference is the device without the field plates. The  $R_{\text{ON}}$  values are in the range  $11.1\text{--}12 \text{ m}\Omega\cdot\text{cm}^2$ . As expected, these were higher than SBDs on the same wafer, which had values in the range  $8.5\text{--}9.4 \text{ m}\Omega\cdot\text{cm}^2$  and on-voltage of  $0.71\text{--}0.75 \text{ V}$ . The HJDs had  $V_{\text{ON}}$  values of  $2.3\text{--}2.4 \text{ V}$ , as shown in the linear plots of Fig. 8. The leakage current of T5 Schottky diode is lower than that of the reference Schottky diode, but the breakdown voltage of Ref SBD is higher. Generally, the increased leakage current of the devices with the edge termination is due to the increased carrier concentration after PECVD. Meanwhile, the edge termination significantly limited the leakage current when

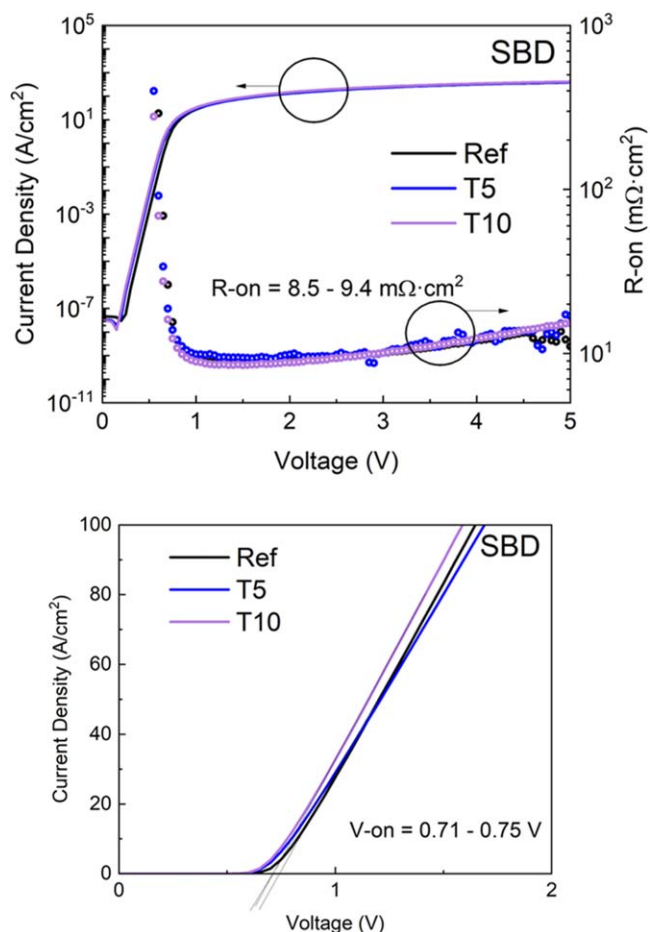


**Figure 10.** Schottky Barrier Diode forward I-Vs on log (a) or linear (b) scales.

the distance from the edge of the dielectric layer and the contact metal is  $10 \mu\text{m}$  rather than  $5 \mu\text{m}$ , especially in the high-voltage region.

The  $V_B$  values for the HJD were up to  $13.5 \text{ kV}$ , as shown in Fig. 9 (top) for optimized edge termination spacing. The unterminated rectifiers have breakdown voltages in the  $6\text{--}7.9 \text{ kV}$  range. The spread in values originates from spatial variations in drift layer doping and so-called killer defect density, the latter of which are known to add reverse leakage current and restrict the maximum  $V_B$ .<sup>52</sup> The range of breakdown voltages measured over  $1 \text{ cm}^2$  was from  $6.5\text{--}13.5 \text{ kV}$ , showing how sensitive this parameter is to the defect density within the active region.<sup>52–65</sup> Note that the associated SBDs fabricated in the same areas as the HJDs show  $V_B$  values up to  $3.6 \text{ kV}$  with edge termination and  $2.7 \text{ kV}$  without edge termination. For large area HJD devices with  $1 \text{ mm}$  diameter, Fig. 9 (bottom) shows the maximum  $V_B$  were  $7.2 \text{ kV}$  with edge termination and  $3.9 \text{ kV}$  without. The larger area devices have more chance of incorporating crystal defects within the active region and typically will show lower breakdown voltages than small area devices.

To contrast the HJD results from those of the SBDs, Fig. 10 shows the forward I-Vs from the latter on both log and linear scales. The on-resistance and turn-on voltages are lower than for the HJDs, as expected. Figure 11 shows the low bias I-V characteristics at top and the high voltage characteristics at bottom for different configurations. Note the much lower  $V_B$  values for the Schottky rectifiers (between  $\sim 1\text{--}3 \text{ kV}$ ) compared to those from the HJDs.

We measured from  $9\text{--}15$  devices for each condition, over an area of  $\sim 1 \text{ cm}^2$  in each case. Table II summarizes the values obtained for the different spacings on both the HJD and SBD. Note the huge increase for the HJD compared to the SBD, which had  $V_B$  of  $2.7 \text{ kV}$

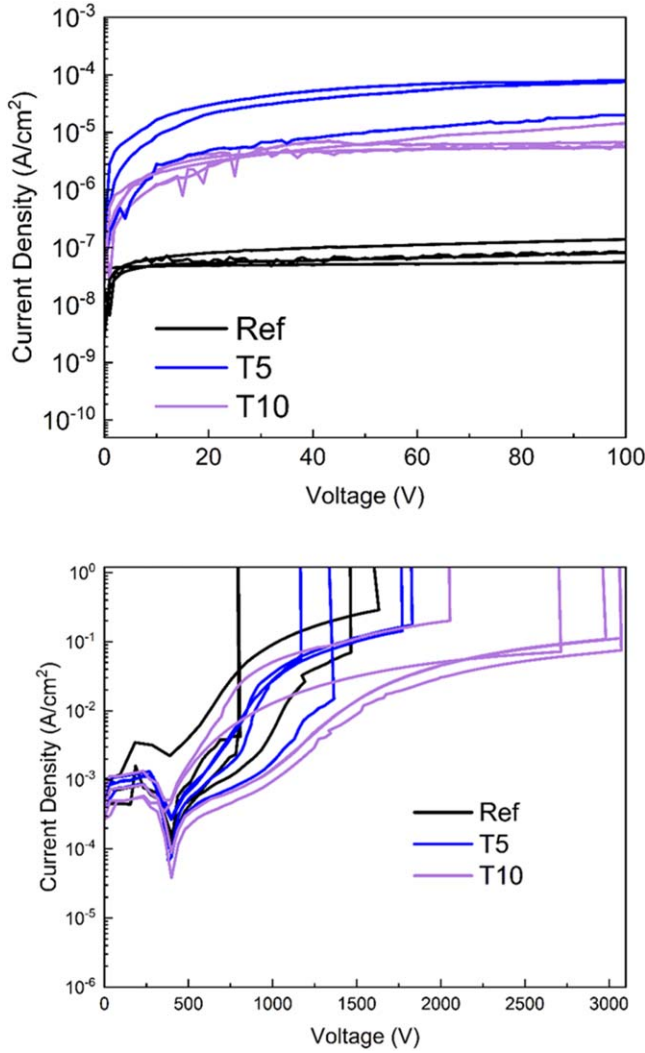


**Figure 11.** Schottky Barrier Diode low bias (a) and high bias (b) reverse I-Vs.

for unterminated devices and 3.6 kV for optimized edge termination. For punch-through conditions as is the case in our devices, the  $V_B$  is given by<sup>72,73</sup>

$$V_B = \varepsilon W_{PT} - \left( \frac{eN_D}{2\varepsilon} \right) W_{PT}^2$$

where  $W_{PT}$  is the depletion depth at punch-through,  $N_D$  is the doping and  $\varepsilon$  the dielectric permittivity. The term  $\left( \frac{eN_D}{2\varepsilon} \right) W_{PT}^2$  can be neglected as its value is  $\sim 10^{-23}$ . The average electric field strength in unterminated HJD is  $\sim 4.4 \text{ MV.cm}^{-1}$  and increases to  $7.5 \text{ MV.cm}^{-1}$  in the edge terminated structures. The power figures of merit  $V_B^2/R_{ON}$  were  $15.2 \text{ GW cm}^{-2}$  for optimized HJD of  $100 \mu\text{m}$  diameter with edge termination and  $5.6 \text{ GW cm}^{-2}$  for unterminated devices. Based on our TCAD simulation, breakdown occurs in the  $\text{Ga}_2\text{O}_3$ . The maximum electric fields are  $\sim 8$ , 6 and 4 MV in  $\text{Ga}_2\text{O}_3$ , NiO and SiNx, respectively. The NiO layers significantly spread the electric field crowding in our design. The dimensions of the field plate are important, with the T10 design being much more effective than the T5. For the large diameter (1 mm) devices, the maximum power FOM was  $0.65 \text{ GW cm}^{-2}$  for edge termination structures.

To place the work in context, Fig. 12 shows a compilation of the reported values of  $V_B$  and  $R_{ON}$  in the literature for small area devices (diameters of  $50\text{--}150 \mu\text{m}$ ), along with the theoretical values for SiC,

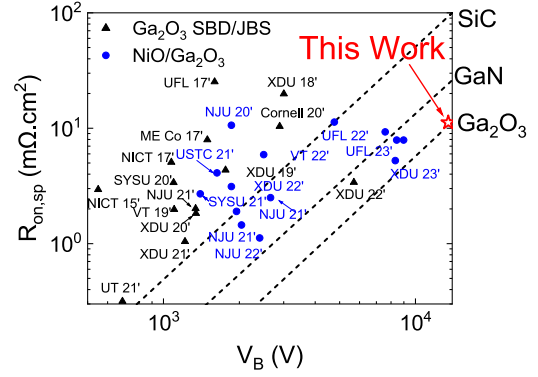


**Figure 12.** Compilation plot of  $R_{on}$  vs  $V_B$  from the reported literature for small diameter ( $50\text{--}150 \mu\text{m}$ )  $\text{Ga}_2\text{O}_3$  HJDs and SBDs.

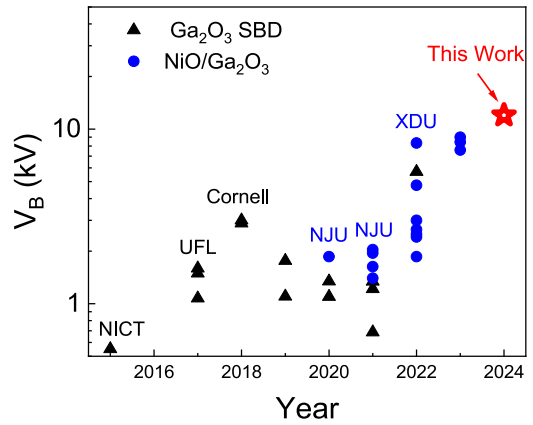


**Figure 13.** Plot of  $V_B$  versus year for small diameter ( $50\text{--}150 \mu\text{m}$ )  $\text{Ga}_2\text{O}_3$  SBDs and HJDs.

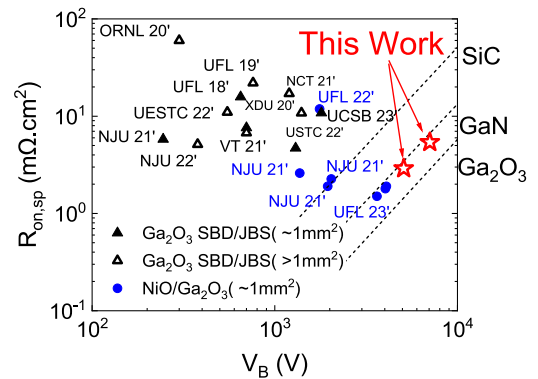


**Figure 14.** Compilation plot of  $R_{on}$  vs  $V_B$  from the reported literature of large diameter ( $\geq 1 \text{ mm}$ )  $\text{Ga}_2\text{O}_3$  HJDs and SBDs.

**Table II.** Maximum  $V_B$  for 15  $\mu\text{m}$  SBD and HJD with diameter  $100 \mu\text{m}$ . Ref is without edge termination.

Voltage (kV)	Ref	T = 5 $\mu\text{m}$	T = 10 $\mu\text{m}$
SBD	2.7	3.4	3.6
HJD	7.9	8.4	13.5

GaN and  $\beta\text{-Ga}_2\text{O}_3$ . This type of commonly shown representation of the advancement of power device technology has a typical trend of device performance being well short of the theoretical maximum in the early stages of development, but improving with time as growth,



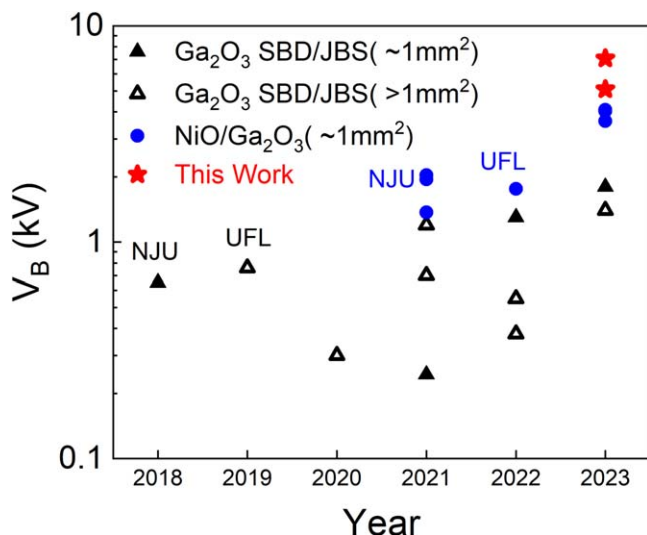


**Figure 15.** Plot of  $V_B$  versus year for large diameter ( $\geq 1$  mm) Ga<sub>2</sub>O<sub>3</sub> SBDs and HJDs.

device design and fabrication are all optimized. There are now numerous demonstrations of  $\beta$ -Ga<sub>2</sub>O<sub>3</sub> rectifiers having performance beyond the 1D limit of GaN and SiC. Our devices are close to the expected maximum for  $\beta$ -Ga<sub>2</sub>O<sub>3</sub>, although these plots are subject to uncertainty due to the actual breakdown field still being uncertain in Ga<sub>2</sub>O<sub>3</sub>. The progress in small diameter Ga<sub>2</sub>O<sub>3</sub> rectifiers is also shown by Fig. 13, which shows the  $V_B$  values as a function of publication date. The introduction of the NiO/Ga<sub>2</sub>O<sub>3</sub> heterojunction has provided a major impetus to this progress.

Corresponding plots for large area ( $\geq 1$  mm diameter) rectifiers are shown in Figs. 14 and 15. Note that the results are still significantly below the theoretical limits of Ga<sub>2</sub>O<sub>3</sub>, reflecting the greater difficulty in overcoming the presence of defects in the active regions of the devices. The performance is still greater than that of GaN and SiC.

### Summary and Conclusions

In summary, the advances in the growth of the HVPE drift layers are partially responsible for the rapid increase in  $V_B$  values for vertical Ga<sub>2</sub>O<sub>3</sub> rectifiers reported over the past 5 years. For example, devices fabricated on 10  $\mu$ m thick drift layers under the same conditions as the devices reported in this paper showed maximum breakdown of 8.9 kV, which also corresponds to a breakdown field in the range of 7.9 MV.cm<sup>-1</sup>. The ability to go to thicker layers brings the substantial increase in  $V_B$  to 13.5 kV. The NiO deposition conditions are crucial to achieving high breakdown voltage in the devices, as well as the design of the edge termination. We established an epitaxial relationship between NiO film and  $\beta$ -Ga<sub>2</sub>O<sub>3</sub> substrate with the [110] zone axis of cubic NiO matches well with [010] zone axis of monoclinic  $\beta$ -Ga<sub>2</sub>O<sub>3</sub> and (001) plane growth surface of  $\beta$ -Ga<sub>2</sub>O<sub>3</sub> roughly matches with ( $\bar{1}10$ ) surface of NiO. Optimized design ensures the breakdown occurs in the Ga<sub>2</sub>O<sub>3</sub> and not in the NiO or dielectric field plates. It is also worth noting that the exact breakdown voltage for Ga<sub>2</sub>O<sub>3</sub> is not firmly established, with some quoting values up to 15 MV.cm<sup>-1</sup>.<sup>72-77</sup> If true, those would suggest that 15 kV devices might be possible with minor improvements to the existing growth and processing capabilities for Ga<sub>2</sub>O<sub>3</sub>. Of course, there is still much to be developed in terms of thermal management of such devices.<sup>78</sup>

### Acknowledgments

The work at UF was performed as part of Interaction of Ionizing Radiation with Matter University Research Alliance (IIRM-URA), sponsored by the Department of the Defense, Defense Threat Reduction Agency under award HDTRA1-20-2-0002. The content

of the information does not necessarily reflect the position or the policy of the federal government, and no official endorsement should be inferred. The authors at National Yang Ming Chiao.

Tung University would like to acknowledge the National Science and Technology Council, Taiwan, for their financial support under Grant No. NSTC 112-2628-E-A49-015.

### ORCID

Jian-Sian Li <https://orcid.org/0000-0002-2817-7612>

Hsiao-Hsuan Wan <https://orcid.org/0000-0002-6986-8217>

Chao-Ching Chiang <https://orcid.org/0000-0002-0447-8170>

Stephen J. Pearton <https://orcid.org/0000-0001-6498-1256>

### References

1. K. Konishi, K. Goto, H. Murakami, Y. Kumagai, A. Kuramata, S. Yamakoshi, and M. Higashiwaki, *Appl. Phys. Lett.*, **110**, 103506 (2017).
2. M. H. Wong and M. Higashiwaki, *IEEE Trans. Electron Devices*, **67**, 3925 (2020).
3. X. Lu, Y. X. Deng, Y. L. Pei, Z. M. Chen, and G. Wang, *J. Semicond.*, **44**, 061802 (2023).
4. A. J. Green et al., *APL Mater.*, **10**, 029201 (2022).
5. S. J. Pearton, F. Ren, M. Tadjer, and J. Kim, *J. Appl. Phys.*, **124**, 220901 (2018).
6. C. Wang, J. Zhang, S. Xu, C. Zhang, Q. Feng, Y. Zhang, J. Ning, S. Zhao, H. Zhou, and Y. Hao, *J. Phys. D: Appl. Phys.*, **54**, 243001 (2021).
7. Y. Kokubun, S. Kubo, and S. Nakagomi, *Appl. Phys. Express*, **9**, 091101 (2016).
8. Y. Deng et al., *Appl. Surf. Sci.*, **622**, 156917 (2023).
9. M. I. Pintor-Monroy, D. Barrera, B. L. Murillo-Borjas, F. J. Ochoa-Estrella, J. W. P. Hsu, and M. A. Quevedo-Lopez, *ACS Appl. Mater. Interfaces*, **10**, 38159 (2018).
10. X. Xia, J.-S. Li, C.-C. Chiang, T. J. Yoo, F. Ren, H. Kim, and S. J. Pearton, *J. Phys. D: Appl. Phys.*, **55**, 385105 (2022).
11. H. Gong, X. Chen, Y. Xu, Y. Chen, F. Ren, B. Liu, S. Gu, R. Zhang, and J. Ye, *IEEE Trans. Electron Devices*, **67**, 3341 (2020).
12. S. Sharma, K. Zeng, S. Saha, and U. Singiseti, *IEEE Electron Device Lett.*, **41**, 836 (2020).
13. J. Z. P. Dong et al., *Nat. Commun.*, **13**, 3900 (2022).
14. P. Dong, J. Zhang, Q. Yan, Z. Liu, P. Ma, H. Zhou, and Y. Hao, *IEEE Electron Device Lett.*, **43**, 765 (2022).
15. J.-S. Li, C.-C. Chiang, X. Xia, T. Jinsoo Yoo, F. Ren, H. Kim, and S. J. Pearton, *Appl. Phys. Lett.*, **121**, 042105 (2022).
16. S. Roy, A. Bhattacharyya, P. Ranga, H. Splawn, J. Leach, and S. Krishnamoorthy, *IEEE Electron Device Lett.*, **42**, 1140 (2021).
17. A. Bhattacharyya, S. Sharma, F. Alema, P. Ranga, S. Roy, C. Peterson, G. Seryogin, A. Osinsky, U. Singiseti, and S. Krishnamoorthy, *Appl. Phys. Express*, **15**, 061001 (2022).
18. K. D. Chabak et al., *Semicond. Sci. Technol.*, **35**, 013002 (2020).
19. Z. Hu et al., *Appl. Phys. Lett.*, **113**, 122103 (2018).
20. R. Sharma, M. Xian, C. Fares, M. E. Law, M. Tadjer, K. D. Hobart, F. Ren, and S. J. Pearton, *J. Vac. Sci. Technol. A*, **39**, 013406 (2021).
21. W. Li, D. Saraswat, Y. Long, K. Nomoto, D. Jena, and H. G. Xing, *Appl. Phys. Lett.*, **116**, 192101 (2020).
22. C. Liao et al., *IEEE Trans. Electron Devices*, **69**, 5722 (2022).
23. M. Xiao et al., *IEEE Trans. Power Electron.*, **36**, 8565 (2021).
24. X. Lu, X. Zhou, H. Jiang, K. Wei Ng, Z. Chen, Y. Pei, K. May, Lau, and G. Wang, *IEEE Electron Device Lett.*, **41**, 449 (2020).
25. C. Wang et al., *IEEE Electron Device Lett.*, **42**, 485 (2021).
26. Q. Yan, H. Gong, H. Zhou, J. Zhang, J. Ye, Z. Liu, C. Wang, X. Zheng, R. Zhang, and Y. Hao, *Appl. Phys. Lett.*, **120**, 092106 (2022).
27. H. H. Gong, X. H. Chen, Y. Xu, F.-F. Ren, S. L. Gu, and J. D. Ye, *Appl. Phys. Lett.*, **117**, 022104 (2020).
28. H. Gong et al., *IEEE Trans. Power Electron.*, **36**, 12213 (2021).
29. H. H. Gong et al., *Appl. Phys. Lett.*, **118**, 202102 (2021).
30. W. Hao, Q. He, K. Zhou, G. Xu, W. Xiong, X. Zhou, G. Jian, C. Chen, X. Zhao, and S. Long, *Appl. Phys. Lett.*, **118**, 043501 (2021).
31. F. Zhou et al., *IEEE Trans. Power Electron.*, **37**, 1223 (2022).
32. J. S. Li, H. H. Wan, C. C. Chiang, X. Xia, T. Yoo, H. Kim, F. Ren, and S. J. Pearton, *Crystals*, **13**, 886 (2023).
33. J. Zhang et al., *ACS Appl. Electron. Mater.*, **2**, 456 (2020).
34. Y. Wang et al., *IEEE Trans. Power Electron.*, **37**, 3743 (2022).
35. H. Zhou, S. Zeng, J. Zhang, Z. Liu, Q. Feng, S. Xu, J. Zhang, and Y. Hao, *Crystals*, **11**, 1186 (2021).
36. B. Wang, M. Xiao, J. Spencer, Y. Qin, K. Sasaki, M. J. Tadjer, and Y. Zhang, *IEEE Electron Device Lett.*, **44**, 221 (2023).
37. F. Zhou et al., *Appl. Phys. Lett.*, **119**, 262103 (2021).
38. J. Yang, F. Ren, Y.-T. Chen, Y.-T. Liao, C.-W. Chang, J. Lin, M. J. Tadjer, S. J. Pearton, and A. Kuramata, *IEEE J. Electron Devices Soc.*, **7**, 57 (2019).
39. J.-S. Li, C.-C. Chiang, X. Xia, F. Ren, and S. J. Pearton, *J. Vac. Sci. Technol. A*, **40**, 063407 (2022).
40. Y. Qin, Z. Wang, K. Sasaki, J. Ye, and Y. Zhang, *Jpn. J. Appl. Phys.*, **62**, SF0801 (2023).
41. Z. Wang et al., *IEEE Trans. Electron Devices*, **69**, 981 (2022).
42. M. Ji, N. R. Taylor, I. Kravchenko, P. Joshi, T. Aytug, L. R. Cao, and M. P. Paranthaman, *IEEE Trans. Power Electron.*, **36**, 41 (2021).



43. H. Gong, F. Zhou, X. Yu, W. Xu, F.-F. Ren, S. Gu, H. Lu, J. Ye, and R. Zhang, *IEEE Electron Device Lett.*, **43**, 773 (2022).
44. B. Wang, M. Xiao, Z. Zhang, Y. Wang, Y. Qin, Q. Song, G.-Q. Lu, K. Ngo, and Y. Zhang, *IEEE Trans. Electron Devices*, **70**, 633 (2023).
45. F. Otsuka, H. Miyamoto, A. Takatsuka, S. Kunori, K. Sasaki, and A. Kuramata, *Appl. Phys. Express*, **15**, 016501 (2022).
46. Y. Lv et al., *IEEE Trans. Power Electron.*, **36**, 6179 (2021).
47. W. Hao et al., *IEEE Trans. Electron Devices*, **70**, 2129 (2023).
48. J.-S. Li, C.-C. Chiang, X. Xia, H.-H. Wan, F. Ren, and S. J. Pearton, *J. Vac. Sci. Technol. A*, **41**, 043404 (2023).
49. S. Sdoeung, K. Sasaki, K. Kawasaki, J. Hirabayashi, A. Kuramata, and M. Kasu, *Jpn. J. Appl. Phys.*, **62**, SF1001 (2023).
50. B. Wang, M. Xiao, J. Knoll, C. Buttay, K. Sasaki, C. Dimarino, and Y. Zhang, *IEEE Electron Device Lett.*, **42**, 1132 (2021).
51. J. S. Li, C. C. Chiang, X. Xia, H. Hsuan Wan, F. Ren, and S. J. Pearton, *J. Mater. Chem. C*, **11**, 7750 (2023).
52. S. Sdoeung, Y. Otsubo, K. Sasaki, A. Kuramata, and M. Kasu, *Appl. Phys. Lett.*, **123**, 122101 (2023).
53. M. I. Chaman, K. Hoshikawa, S. Sdoeung, and M. Kasu, *Jpn. J. Appl. Phys.*, **61**, 055501 (2022).
54. M. Kasu, K. Hanada, T. Moribayashi, A. Hashiguchi, T. Oshima, T. Oishi, K. Koshi, K. Sasaki, A. Kuramata, and O. Ueda, *Jpn. J. Appl. Phys.*, **55**, 1202BB (2016).
55. M. Kasu, T. Oshima, K. Hanada, T. Moribayashi, A. Hashiguchi, T. Oishi, K. Koshi, K. Sasaki, A. Kuramata, and O. Ueda, *Jpn. J. Appl. Phys.*, **56**, 091101 (2017).
56. T. Oshima, A. Hashiguchi, T. Moribayashi, K. Koshi, K. Sasaki, A. Kuramata, O. Ueda, T. Oishi, and M. Kasu, *Jpn. J. Appl. Phys.*, **56**, 086501 (2017).
57. O. Ueda, N. Ikenaga, K. Koshi, K. Iizuka, A. Kuramata, K. Hanada, T. Moribayashi, S. Yamakoshi, and K. Kasu, *Jpn. J. Appl. Phys.*, **55**, 1202BD (2016).
58. S. Masuya, K. Sasaki, A. Kuramata, S. Yamakoshi, O. Ueda, and M. Kasu, *Jpn. J. Appl. Phys.*, Part **158**, 055501 (2019).
59. K. Hanada, T. Moribayashi, T. Uematsu, S. Masuya, K. Koshi, K. Sasaki, A. Kuramata, O. Ueda, and M. Kasu, *Jpn. J. Appl. Phys.*, **55**, 030303 (2016).
60. E. Ohba, T. Kobayashi, M. Kado, and K. Hoshikawa, *Jpn. J. Appl. Phys.*, **55**, 1202BF (2016).
61. O. Ueda, K. Kasu, and H. Yamaguchi, *Jpn. J. Appl. Phys.*, **61**, 050101 (2022).
62. S. Sdoeung, K. Sasaki, K. Kawasaki, J. Hirabayashi, A. Kuramata, T. Oishi, and M. Kasu, *Appl. Phys. Lett.*, **117**, 022106 (2020).
63. S. Sdoeung, K. Sasaki, K. Kawasaki, J. Hirabayashi, A. Kuramata, and M. Kasu, *Jpn. J. Appl. Phys.*, **62**, 071001 (2023).
64. K. Goto, H. Murakami, A. Kuramata, S. Yamakoshi, M. Higashiwaki, and Y. Kumagai, *Appl. Phys. Lett.*, **120**, 102102 (2022).
65. S. Sdoeung, K. Sasaki, K. Kawasaki, J. Hirabayashi, A. Kuramata, and M. Kasu, *Appl. Phys. Lett.*, **120**, 092101 (2022).
66. A. Kuramata, K. Koshi, S. Watanabe, Y. Yamaoka, T. Masui, and S. Yamakoshi, *Jpn. J. Appl. Phys.*, **55**, 1202A2 (2016).
67. C.-C. Chiang, X. Xia, J.-S. Li, F. Ren, and S. J. Pearton, *Appl. Surf. Sci.*, **631**, 157489 (2023).
68. P. H. Carey, J. Yang, F. Ren, R. Sharma, M. Law, and S. J. Pearton, *ECS J. Sol. State Sci. Technol.*, **8**, Q3221 (2019).
69. C. C. Chiang, J. S. Li, H. H. Wa, F. Ren, and S. J. Pearton, *Crystals*, **13**, 1124 (2023).
70. J. B. Varley, J. R. Weber, A. Janotti, and C. G. van de Walle, *Appl. Phys. Lett.*, **97**, 142106 (2010).
71. A. Portoff, A. Venzie, M. Stavola, W. B. Fowler, E. Glaser, and S. J. Pearton, *J. Appl. Phys.*, **134**, 045701 (2023).
72. B. J. Baliga, *Fundamentals of Power Semiconductor Devices* 2nd ed. (Springer, New York) (2018).
73. O. Slobodyan, J. Flicker, J. Dickerson, J. Shoemaker, A. Binder, T. Smith, S. Goodnick, R. Kaplar, and M. Hollis, "Analysis of the dependence of critical electric field on semiconductor bandgap," *J. Mater. Res.*, **37**, 849 (2022).
74. R. Kaplar, H. Zhao, K. Goretta, N. Johnson, M. Hollis, T. Ivanov, A. Lelis, D. Pavlidis, and K. Jones, *Ultra-Wide Bandgap Semiconductors Workshop III*, ed. K. A. Jones ARL-SR-0448 (2021).
75. R. Kaplar, *Ultra Wide Bandgap Semiconductors: Opportunities and Challenges Ultra Fast Triggered Semiconductor Devices Workshop*, (Washington DC) (2022).
76. L.-M. Wang, "Relationship between intrinsic breakdown field and bandgap of materials," *25th IEEE Int. Conf. on Microelec. (2006), Belgrade, Serbia and Montenegro*, 1st ed. (2006).
77. M. Hollis, O. Slobodyan, J. Flicker, J. Dickerson, A. Binder, T. Smith, and R. Kaplar, "Dependence of critical electric field on semiconductor bandgap—an analytical study," *MRS Fall Meeting, Boston, MA* (2020).
78. Y. Qin, B. Albano, J. Spencer, J. S. Lundh, B. Wang, C. Buttay, M. Tadjer, C. DiMarino, and Y. Zhang, *J. Phys. D: Appl. Phys.*, **56**, 093001 (2023).